

**ISTITUTO NAZIONALE DI RICERCA METROLOGICA**  
**Repository Istituzionale**

X-ray phase-contrast topography to measure the surface stress and bulk strain in a silicon crystal

*Original*

X-ray phase-contrast topography to measure the surface stress and bulk strain in a silicon crystal / Massa, E.; Sasso, C. P.; Fretto, M.; Martino, L.; Mana, G.. - In: JOURNAL OF APPLIED CRYSTALLOGRAPHY. - ISSN 1600-5767. - 53:5(2020), pp. 1195-1202. [10.1107/s1600576720009267]

*Availability:*

This version is available at: 11696/63870 since: 2021-01-26T16:49:31Z

*Publisher:*

International Union of Crystallography - Wiley

*Published*

DOI:10.1107/s1600576720009267

*Terms of use:*

This article is made available under terms and conditions as specified in the corresponding bibliographic description in the repository

*Publisher copyright*

(Article begins on next page)



## X-ray phase-contrast topography to measure the surface stress and bulk strain in a silicon crystal

**E. Massa, C. P. Sasso, M. Fretto, L. Martino and G. Mana**

*J. Appl. Cryst.* (2020). **53**, 1195–1202



**IUCr Journals**  
CRYSTALLOGRAPHY JOURNALS ONLINE

Copyright © International Union of Crystallography

Author(s) of this article may load this reprint on their own web site or institutional repository provided that this cover page is retained. Republication of this article or its storage in electronic databases other than as specified above is not permitted without prior permission in writing from the IUCr.

For further information see <https://journals.iucr.org/services/authorrights.html>

Received 29 April 2020

Accepted 7 July 2020

Edited by V. Holý, Charles University, Prague,  
Czech Republic and CEITEC at Masaryk  
University, Brno, Czech Republic

**Keywords:** X-ray interferometry; solid-state  
surface stress; X-ray phase-contrast topography;  
lattice strain measurement; lattice parameters.

# X-ray phase-contrast topography to measure the surface stress and bulk strain in a silicon crystal

E. Massa, C. P. Sasso,\* M. Fretto, L. Martino and G. Mana

INRIM – Istituto Nazionale di Ricerca Metrologica, Strada delle Cacce 91, 10135 Torino, Italy. \*Correspondence e-mail:  
c.sasso@inrim.it

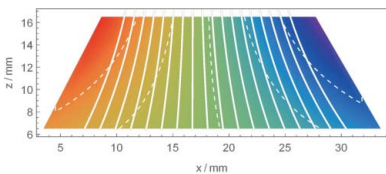
The measurement of the Si lattice parameter by X-ray interferometry assumes the use of strain-free crystals, which might not be true because of intrinsic stresses due to surface relaxation, reconstruction and oxidation. X-ray phase-contrast topography was used to investigate the strain sensitivity to the finishing, annealing and coating of interferometer crystals. The topography capabilities were assessed by measuring the lattice strain due to films of copper deposited on the interferometer mirror crystal. A by-product has been the measurement of the surface stresses after complete relaxation of the coatings.

## 1. Introduction

A separated single-crystal X-ray interferometer was previously used by our group to measure the lattice parameter of silicon to within a fractional uncertainty approaching  $1 \text{ nm m}^{-1}$  (Massa *et al.*, 2015). The interferometer was ground by diamond tools and chemically etched to remove surface damage (Zawisky *et al.*, 2010). If too little material is etched away, lattice strains prevent the interferometer operation; if too much, the interferometer geometry degrades, and the fringe contrast is lost.

Phase-contrast topography by X-ray interferometry is a well known tool to study defects and strains in single crystals (Bonse *et al.*, 1976; Ohler *et al.*, 1999; Fodchuk & Raransky, 2003; Pushin *et al.*, 2007; Miao *et al.*, 2016). We have used it to investigate the effect of surface finishing on interferometer operation (Bergamin *et al.*, 2000). Our goal was to optimize the manufacturing and to trade off between no surface damage (via chemical etching) and accurate geometry (via mechanical grinding). The test interferometers were etched step by step and etching was stopped when it neither improved the fringe contrast nor reduced the lattice strain. The procedure that was found to be optimal prescribes a first chemical etching, then machining with the finest diamond grinding wheel to correct about  $10 \mu\text{m}$  etch errors, and a final etching to a depth of about  $50 \mu\text{m}$ .

These investigations did not prove that surface stresses due to oxidation, relaxation and reconstruction did not affect the lattice-parameter value (Kessler *et al.*, 1999). The magnitude of this effect was estimated by a finite element analysis, where the surface stress (a fundamental property of the crystal interface with the environment) was modelled by an elastic membrane having a hypothetical  $1 \text{ N m}^{-1}$  tensile strength (Quagliotti *et al.*, 2013). We also calculated the surface stress by density functional theory (Melis *et al.*, 2016) and found a value exceeding  $1 \text{ N m}^{-1}$ , which potentially jeopardizes the measurement accuracy.



© 2020 International Union of Crystallography

Prompted by this treatment and the observations of increased visibility and reduced strains after annealing reported by Heacock *et al.* (2018, 2019), we carried out new topographic investigations of the annealing and etching effects on interferometer crystals. To test the capabilities of phase-contrast topography, we measured the strain in the crystal bulk caused by nanometric films of copper deposited on an interferometer crystal. As a by-product, we obtained the in-plane mean stress in copper films on a silicon substrate.

Phase-contrast imaging proved to be an extremely sensitive technique to measure stress in films only a few nanometres thick. Since it affects the design, processing, performance, reliability and lifetime of advanced materials and components, the measurement of stress in thin films and coatings is also a crucial issue in materials science and technology (Sharma *et al.*, 2015; Abadias *et al.*, 2018).

## 2. Experimental setup

Fig. 1 shows the apparatus for phase-contrast topography. A first crystal (splitter) splits 17 keV X-rays from a fixed anode ( $0.1 \times 10$ ) mm $^2$  Mo  $K\alpha_1$  source, which are recombined, via a mirror-like crystal, by a third crystal (analyser). X-rays are roughly collimated by a ( $0.5 \times 16$ ) mm $^2$  slit placed in front of the interferometer. The interference fringes are imaged onto a multi-anode photomultiplier tube through a vertical 15 mm pile of eight 1 mm NaI(Tl) scintillators, spaced by 1 mm shades.

The interferometer blades (splitter S, mirror M and analyser A) are ( $35 \times 18 \times 0.8$ ) mm $^3$ , spaced 10 mm apart, and protrude from a common base (see Fig. 2). Since the X-ray source and detector are 0.8 and 0.3 m apart from the mirror and the beam width at the mirror is 1 mm, the images of the scintillator pixels projected on the mirror are, on average, ( $1 \times 3$ ) mm $^2$ . The projected image of the 15 mm scintillator pile is 13 mm in height, from the mirror top downwards.

As shown in Fig. 1, we surveyed a ( $30 \times 10$ ) mm $^2$  area of the blades by moving the interferometer in 0.5 mm steps along the

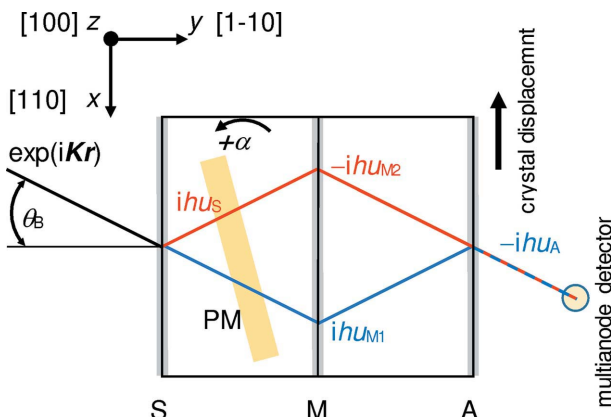


**Figure 1**  
X-ray phase-contrast topography. S, splitter; M, mirror; A, analyser; PM, phase modulator. The X-ray paths are drawn in red (RRT) and blue (TRR). The Bragg angle is not to scale; its actual value is about  $11^\circ$ . The phase delay of each reflection is given. The X-ray crossings with the mirror are spaced by 4 mm.

x axis and detecting the interference fringes one after the other in 61 adjacent ( $1 \times 13$ ) mm $^2$  vertical (overlapping) slabs. Each vertical slab is further subdivided into eight (overlapping) pixels of ( $1 \times 3$ ) mm $^2$ , corresponding to the photomultiplier channels. The result is a discrete image of ( $61 \times 8$ ) pixels. A more detailed description of the measurement procedure is given by Bergamin *et al.* (2000).

## 3. Measurement equation

According to density functional theory calculations (Melis *et al.*, 2016), the surface stress strains the interferometer blades uniformly, apart from a few lattice planes at the surface. Since the thickness of this strained layer (about 2 nm) is much smaller than the *Pendellösung* length (about 30  $\mu\text{m}$ ), a perfect-crystal boundary can substitute for the transition region (Mana & Palmisano, 2004).

Therefore, in a geometric optics model (with the positive-exponent choice representing a plane wave with positive wavenumber  $K$ , see Fig. 1), each reflection delays the X-ray phase by  $\pm hu_i(x, z)$  (Mana & Vittone, 1997*a,b*), where  $h = 2\pi/d$  is the reciprocal vector,  $d$  is the diffracting-plane spacing, and  $u_i(x, z)$  ( $i = A, M1, M2, S$ ) is the  $x$  component of the displacement field of the splitter, mirror or analyser lattice. The sign is positive if the displacement  $u_i(x, z)$  occurs in the same direction as the  $x$  component of the incident-beam wavevector and negative otherwise. No phase delay occurs in the transmissions.

This is not true if the blade surfaces are differently stressed (Camattari *et al.*, 2020; Ferrari *et al.*, 2020). In this case, there is a strain gradient along the blade depth and the phase difference between the transmitted and reflected rays is set by the displacement field on the entrance surface (Mana & Palmisano, 2004; Apolloni *et al.*, 2008).

The phase delays along the two paths reaching the observation plane – one performing two reflections (R) followed by one transmission (T), the other one transmission followed by two reflections – are thus

$$\phi_{\text{RTT}} = h(u_S - u_{M2}), \quad (1a)$$

$$\phi_{\text{TRR}} = h(u_{M1} - u_A). \quad (1b)$$



**Figure 2**  
Photograph of the X-ray interferometer with a Cu film on the mirror crystal. The film thickness has been increased to make it visible.

Interference occurs because the rays overlap after crossing crystal lattices whose planes are misplaced with respect to one another. The total phase is

$$\phi_u = \phi_{\text{RRT}} - \phi_{\text{TRR}} = h(u_S + u_A - u_{M1} - u_{M2}). \quad (2)$$

A phase modulator, a plastic sheet 1 mm thick, is placed between the splitter and mirror. A simple geometrical analysis shows that – with the positive-exponent choice to represent a plane wave with positive  $K$  (see Fig. 1) – it varies the interference phase by  $K(T_{\text{RRT}} - T_{\text{TRR}})\alpha \simeq -2KT(n-1)\theta_B\alpha$ , where  $\alpha$  is the angle of rotation,  $T$  the thickness of the modulator,  $T_{\text{RRT}}, T_{\text{TRR}}$  the length of the X-ray path through the modulator,  $n < 1$  the index of refraction and  $\theta_B$  the Bragg angle, and the linearization with respect to the rotation angle is valid if  $\alpha \ll 1$  rad.

When the phase modulator is rotated, the moving fringes are detected by each of the eight photomultiplier channels, making it possible to extract the effective displacement field  $u_x = u_S + u_A - u_{M1} - u_{M2}$ . The measurement equation is

$$I_n = I_{0n} [1 + \Gamma_n \cos(\phi_n + \Omega\alpha)], \quad (3)$$

where  $n = 1, 2, \dots, (61 \times 8)$  label the image pixel,  $I_{0n}$  is the average count rate,  $\Gamma_n > 0$  the contrast and  $\Omega = 2KT(1 - n)\theta_B > 0$  the period.

The phases  $\phi_n \in [0, 2\pi]$  in the  $(61 \times 8)$  image pixels were recovered by (nonlinear) least-squares estimations, with the constraints  $\Gamma_n > 0$  and  $\Omega > 0$ . After unwrapping, we found the optimal polynomial regression  $\phi(x, z)$  explaining the  $\phi_n$  data and used it to infer the effective lattice displacement  $u_x(x, z) = \phi(x, z)/(2\pi)$ . The trade-off between underfitting and overfitting was carried out according to the work of Mana *et al.* (2014, 2019).

Finally, we calculated the components  $\epsilon_{xx}(x, z) = \partial_x u_x(x, z)$  (normal strain, the relative variation of lattice spacing) and  $\epsilon_{xz}(x, z) = \partial_z u_x(x, z)$  (shear strain, the lattice-plane rotations about the  $y$  axis) of the strain tensor. Since the fringe phase is recovered only modulo  $2\pi$ , a constant  $u_x(x, z)$  field is undetectable. However, positive phase gradients correspond to displacements of the splitter and analyser lattices in the  $x$  direction of the incident X-rays. The opposite is true for the mirror lattice. Therefore, tensile and compressive strains can be distinguished.

In (2), we neglected minor contributions to the phase, coming from deviations from ideally plane and parallel surfaces of the crystals and phase modulator. They are discussed by Mana & Vittone (1997) and Bergamin *et al.* (2000) and might amount to a few per cent of a period. However, since we are interested in the strain changes after reprocessing of the crystal surfaces, we are looking at the difference in subsequent phase surveys and these constant contributions are mostly irrelevant.

#### 4. Crystal annealing

We surveyed the lattice strain of the interferometer crystal after optimal grinding and etching. Next, the interferometer was annealed in an evacuated tube furnace [the residual

pressure was  $10^{-5}$  mbar (1 mbar = 100 Pa)], at 1073 K for 12 h. Finally, the finishing of the crystal surfaces was reset by re-etching. The sequence of moiré topographies is shown in Fig. 3.

After finding the optimal approximations of the lattice displacement fields (the residual standard deviations are about 3% of the peak-to-peak displacements), we calculated the  $xx$  and  $xz$  components of the strain tensors. Figs. 4 and 5 highlight that the surface finishing plays a role in determining the bulk spacing and tilt of the diffracting planes. Sorted as in Figs. 3 to 5, the mean strains and peak-to-peak variations are

$$\begin{aligned} \overline{\epsilon_{xx}} &= 0^{+4}_{-2} \text{ nm m}^{-1}, & \overline{\epsilon_{xz}} &= +4^{+11}_{-5} \text{ nrad}, \\ \overline{\epsilon_{xx}} &= -3^{+6}_{-11} \text{ nm m}^{-1}, & \overline{\epsilon_{xz}} &= -6^{+1}_{-12} \text{ nrad}, \\ \overline{\epsilon_{xx}} &= -1^{+2}_{-4} \text{ nm m}^{-1}, & \overline{\epsilon_{xz}} &= -1^{+2}_{-4} \text{ nrad}. \end{aligned} \quad (4)$$

While the normal strain did not change significantly, there was an overall alignment of the diffracting planes, indicating that some stress in the base was relieved. Fig. 6 shows that the realignment of the interferometer crystals was significant enough to improve the fringe contrast.

We cannot explain why the annealing made the interferometer performance worse at first and better after another etching. We suspect that annealing relaxed some ‘inner’ stress, but also changed the state of the surfaces. The subsequent etching might have relaxed again the surface stress.

Since, according to (2), four displacement fields superimpose, we cannot give a measure of the strain in any single crystal. If we assume the four fields are uncorrelated, by dividing the observed peak-to-peak strains by two, we can

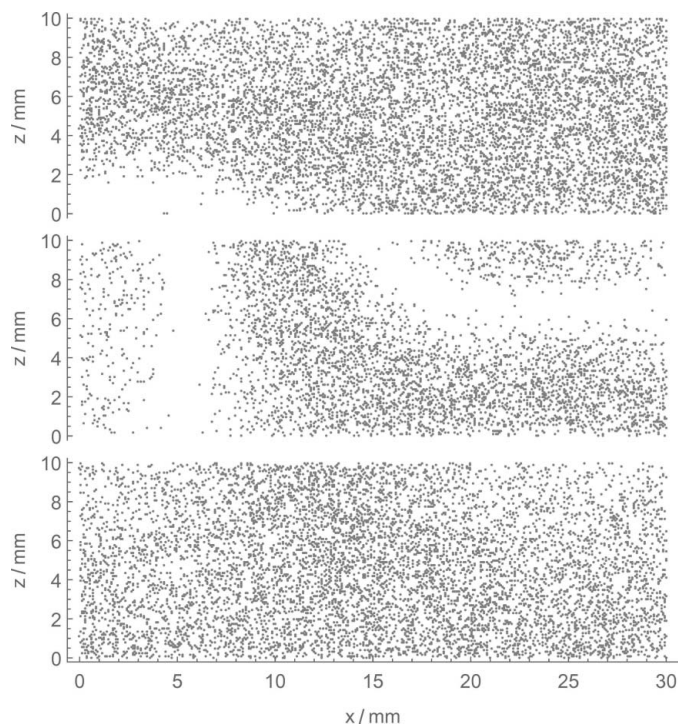


**Figure 3**  
Moiré topographies of the X-ray interferometer after optimal grinding and etching (top), annealing (middle) and re-etching (bottom). The coordinates are relative to the bottom-left corner of the image. The fringe contrast has been artificially enhanced to one to improve visibility.

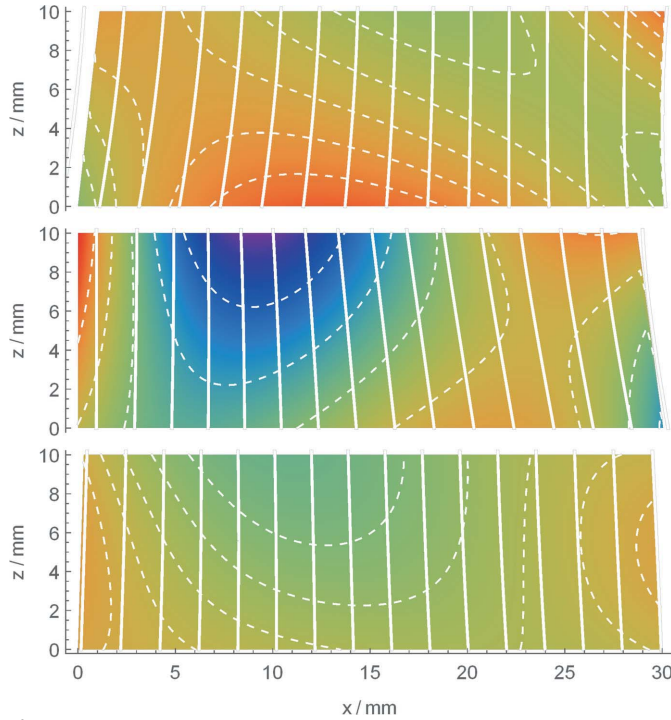


**Figure 4**  
Density plots of the  $xx$  component of the strain tensor inferred from the moiré topographies shown in Fig. 3. From top to bottom: optimal grinding and etching, annealing, and re-etching. The colour scale is from  $-11 \text{ nm m}^{-1}$  (blue) to  $+6 \text{ nm m}^{-1}$  (red). Contour lines are dashed. Solid lines are the lattice planes with distortions magnified. The coordinates are relative to the bottom-left corner of the image.

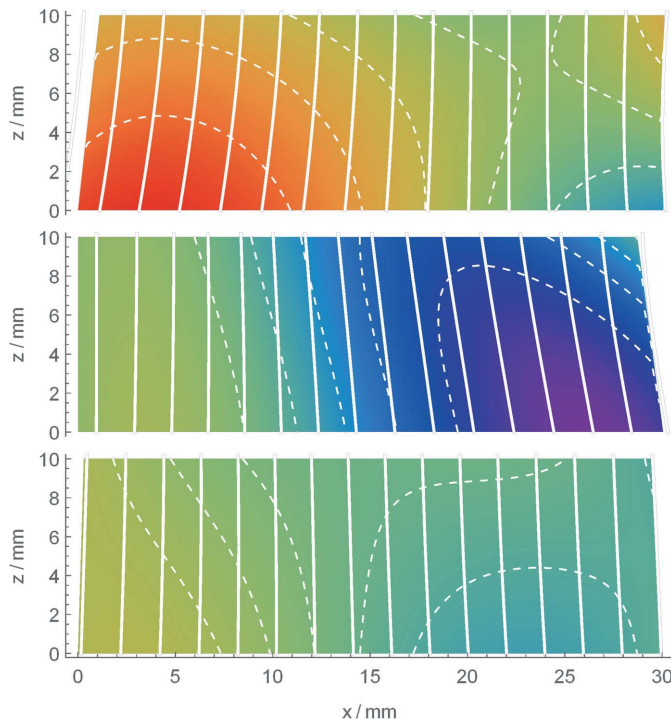


**Figure 5**  
Density plots of the  $xz$  component of the strain tensor inferred from the moiré topographies shown in Fig. 3. From top to bottom: optimal grinding and etching, annealing, and re-etching. The colour scale is from  $-12 \text{ nrad}$  (blue) to  $+11 \text{ nrad}$  (red). Contour lines are dashed. Solid lines are the lattice planes with distortions magnified. The coordinates are relative to the bottom-left corner of the image.

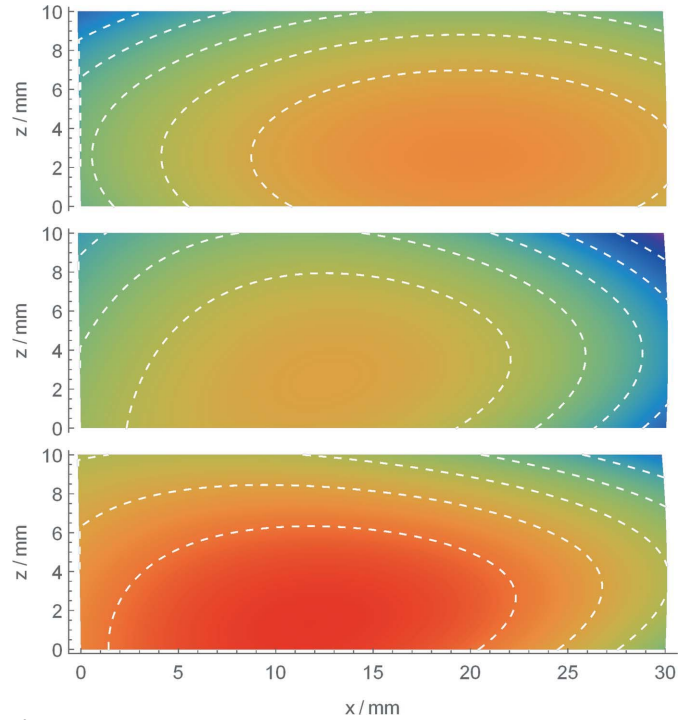


**Figure 6**  
Density plots of the fringe contrast inferred from the moiré topographies shown in Fig. 3. From top to bottom: optimal grinding and etching, annealing, and re-etching. The colour scale is from 14% (blue) to 81% (red). Contour lines are dashed. The coordinates are relative to the bottom-left corner of the image.

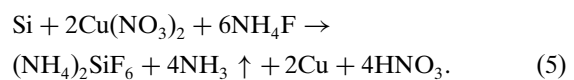
estimate (local) surface effects on the spacing and tilt of the diffracting planes of about  $\pm 1.5 \text{ nm m}^{-1}$  and  $\pm 1.5 \text{ nrad}$ .

As regards the mean strain in a single crystal and measurement of the lattice parameter (Massa *et al.*, 2015; Bartl *et al.*, 2017; Fujii *et al.*, 2017), we might expect a fraction of these effects. We cannot, however, make any specific assertion about this point.

## 5. Crystal coating

To check the capabilities of phase-contrast topography and to gain some preliminary clues on the possible effects of the  $\text{SiO}_2$  surface layer on the lattice parameter, we measured the crystal strain after auto-catalytical coatings of the mirror surface with nanometric films of copper.

The coating (see Fig. 2) was carried out by an electroless galvanic displacement mechanism in a water solution of copper(II) nitrate,  $\text{Cu}(\text{NO}_3)_2$  [ $\rho_{\text{Cu}(\text{NO}_3)_2} = 60 \text{ g l}^{-1}$ ], and ammonium fluoride,  $\text{NH}_4\text{F}$  ( $\rho_{\text{NH}_4\text{F}} = 30 \text{ g l}^{-1}$ ). In this process, the copper plates the silicon surface and, simultaneously, the oxidized silicon is removed by  $\text{HF}^-$  to form water-soluble silicates and a clean interface between the Cu layer and the silicon crystal surface. Therefore, two processes occur together: etching of the silicon surface and plating by copper. The overall stoichiometric reaction is (Mendel & Yang, 1969)



The growth rate and quality of the Cu film depend on the solution composition and temperature. Therefore, we standardized them as well as the plating duration, 10, 20 and 40 s.

### 5.1. Film-thickness measurement

We measured the thickness of the Cu film by coating an optical polished single-crystal Si wafer (with deposition times ranging from 15 to 90 s with 15 s increments) masked so as to create six ( $5 \times 5$ ) mm<sup>2</sup> Cu pads, each bounded by a reference Cu-free area.

After the Cu films were removed by a water solution of iron(III) chloride,  $\text{FeCl}_3$  ( $\rho_{\text{FeCl}_3} = 300 \text{ g l}^{-1}$ ), we used an optical confocal profilometer (Sensofar S Neox Optical Profiler) to measure the steps between the coated and non-coated areas. Since the Cu molar volume is half that of Si and, according to (5), two Cu atoms are substituted for each Si atom removed, the thicknesses of the Cu films were estimated as equal to the observed drops. Fig. 7 shows the results. The exponential fit is only a visual aid to interpolate the data; we do not have any *a priori* model of the growth rate of the copper film.

We prepared the mirror surface by the same etching/coating procedure used for the Si wafer: three increasing deposition times (10 s, 20 s, 40 s) were used to plate the surface with an increasingly thicker copper film. According to Fig. 7, we estimated the thicknesses of the Cu films on the interferometer mirror as  $t_{\text{Cu}} = 1.3$  (4) nm,  $t_{\text{Cu}} = 4$  (1) nm and  $t_{\text{Cu}} = 14$  (3) nm, for deposition times of 10, 20 and 40 s, respectively. The parentheses are a concise notation for the standard uncertainty: the enclosed digit applies to the numeral to its left.

### 5.2. Displacement-field measurement

The displacements of the mirror lattice due to the Cu coatings,  $u_M = (u_{M1} + u_{M2})/2$ , were obtained by subtracting the regression of the pre-coating displacement field from those observed after the coatings, and reversing the sign.

The moiré topographies and displacement fields  $u_M$  are shown in Figs. 8 and 9. The Cu films compress the crystal lattice and the stress increases with the thickness. This

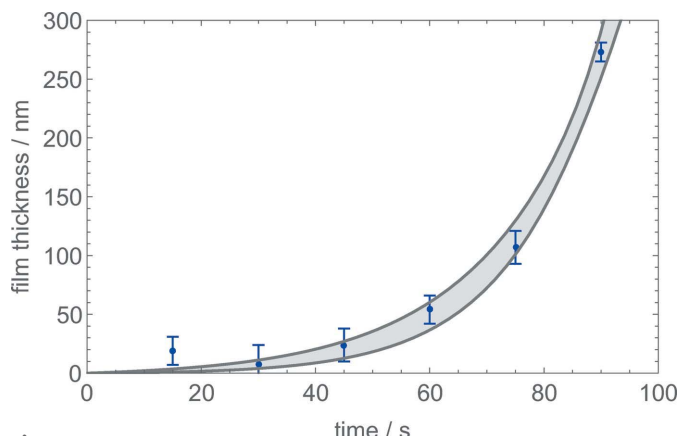


Figure 7

Measured thickness of the Cu film versus the deposition time. Bars are the 95% confidence intervals of the data. The filled area represents the 95% confidence intervals of the exponential fit to the data.

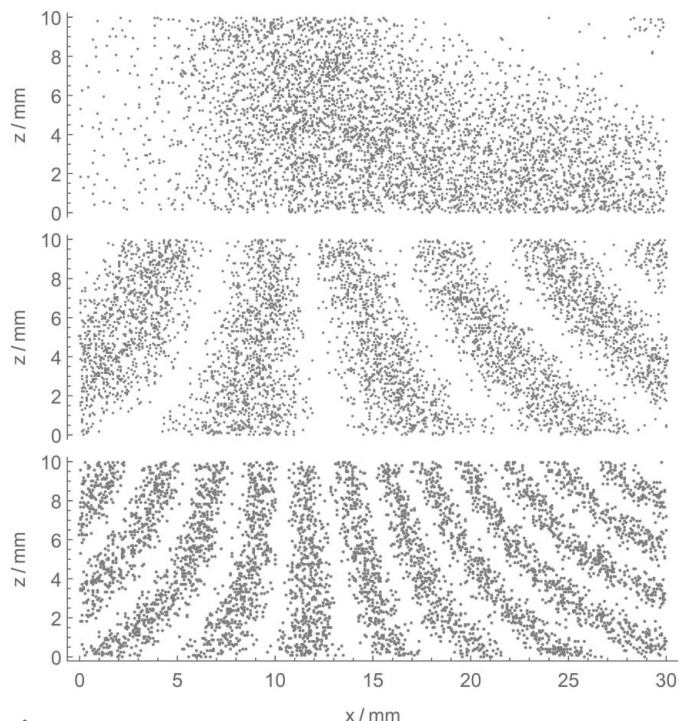


Figure 8

Moiré topographies of the X-ray interferometer after auto-catalytical Cu plating of the mirror crystal. From top to bottom: 1.3 (4), 4 (1) and 14 (3) nm film thickness. The coordinates are relative to the bottom-left corner of the image. The fringe contrast has been set to one to improve visibility.

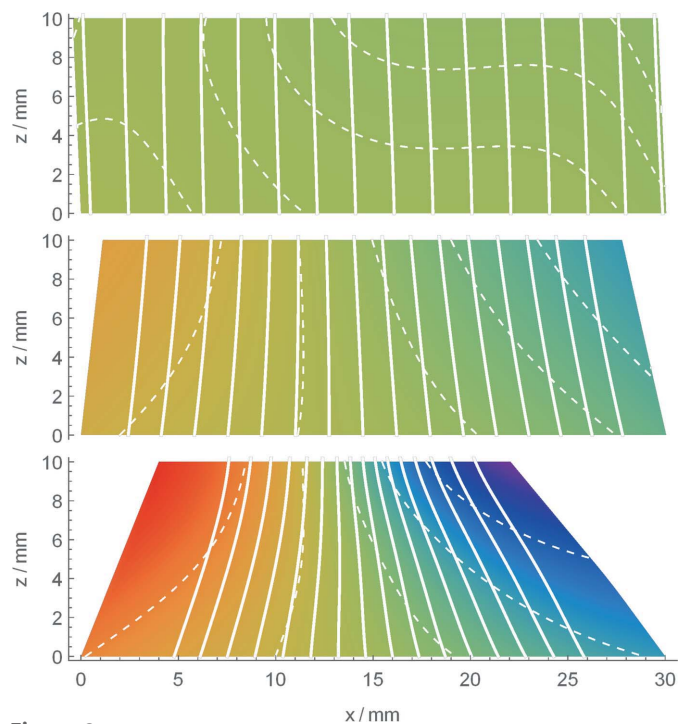


Figure 9

Density plots of the  $u_M(x, z)$  values (polynomial regressions) inferred from the moiré topographies shown in Fig. 8. The coordinates are relative to the bottom-left corner of the image. From top to bottom: 1.3 (4), 4 (1) and 14 (3) nm thickness of the Cu film. The colour scale is from -624 pm (blue) to +486 pm (red), contour lines are dashed, solid lines are the lattice planes with distortions magnified. The residual standard deviations are 4 pm (top), 4 pm (middle) and 6 pm (bottom).

compression is consistent with the tensile stress of the Cu films (developing after growing and relaxation) reported in the literature (Sharma *et al.*, 2015; Abadias *et al.*, 2018).

### 5.3. Surface-stress measurement

To infer the magnitude of the tensile stress of the Cu film, we set up a finite element analysis of the interferometer mirror, modelled as a  $(35 \times 18 \times 0.8)$  mm<sup>3</sup> Si crystal (CSC-IT, 2020). The effect of the film tensile stress, assumed to be equiaxial and uniform, was simulated by a compressive surface stress,  $\tau(t_{\text{Cu}})$ , modelled as forces per unit length (from  $\tau = 1$  N m<sup>-1</sup> to  $\tau = 4.5$  N m<sup>-1</sup>, in variable steps), applied orthogonally to its 12 edges and lying in the crystal surfaces. We set Dirichlet boundary conditions on the bottom surface, specifying null displacements, and used an anisotropic stiffness matrix (Quagliotti *et al.*, 2013).

To realize a digital twin of the experimental setup, the lattice displacement along the  $x$  axis obtained via the finite element analysis,  $u_x(x, z; \tau)$ , was averaged over a pair of  $(1 \times 3)$  mm<sup>2</sup> windows spaced by 4 mm, the separation of the X-ray paths at the interferometer mirror (see Fig. 1). To simulate the experimental  $(61 \times 8)$  images, the window pairs (the image of each scintillator pixel) were shifted vertically by eight 1.25 mm steps and horizontally by 61 0.5 mm steps. Eventually, we found the polynomial regressions explaining the simulated data trading off again between underfitting and

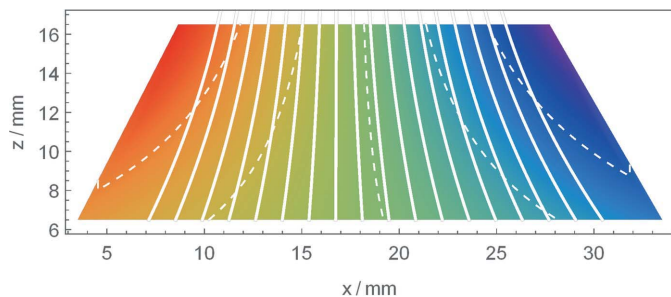


**Figure 10**  
Density plot (polynomial regression) of the simulated lattice displacements,  $u_x(x, z; \tau = 3.5$  N m<sup>-1</sup>). The colour scale is from  $-625$  pm (blue) to  $+460$  pm (red), contour lines are dashed, solid lines are the lattice planes with distortions magnified. The abscissa and ordinate refer to the hypothetical mirror area imaged experimentally.

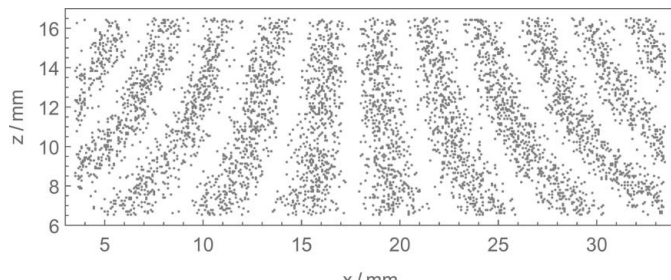


**Figure 11**  
Moiré topography inferred from the simulated displacements shown in Fig. 10. The abscissa and ordinate refer to the hypothetical mirror area imaged experimentally. The fringe contrast has been set to one to improve visibility.

**Table 1**

The surface stress  $\tau$  as a function of the Cu film thickness  $t_{\text{Cu}}$  estimated using both the mean strain at the mirror top,  $\epsilon_{xx}^{\text{top}}$ , and the curvature of the lattice displacement,  $\kappa$ .

	Cu film thickness, $t_{\text{Cu}}$ (nm)	1.3	4	14
Strain at the top				
$\epsilon_{xx}^{\text{top}}$ (pm mm <sup>-1</sup> )	2.3 (2)	16.0 (2)	37.0 (3)	
$\tau$ (N m <sup>-1</sup> )	0.22 (2)	1.55 (2)	3.58 (3)	
Displacement curvature				
$\kappa$ (10 <sup>-12</sup> m <sup>-1</sup> )	0.07 (3)	0.73 (3)	2.03 (6)	
$\tau$ (N m <sup>-1</sup> )	0.16 (7)	1.60 (7)	4.44 (13)	

overfitting according to the work of Mana *et al.* (2014, 2019). The regression of the displacement field for the  $\tau = 3.5$  N m<sup>-1</sup> case is shown in Fig. 10. Fig. 11 shows the moiré topography inferred from this regression.

The similarities between the displacements and fringes depicted in Figs. 10 and 11 and the ones at the bottom of Figs. 8 and 9 are a clear hint that a surface stress of a few N m<sup>-1</sup> is the quantity driving the observed strain of the crystal lattice. The strain magnitude is proportional to the density of the fringes, showing that the digital twin predicts correctly that the crystal is more strained at the free top and that the strain degrades at the bottom, where the crystal base hinders the lattice distortion. With a digital twin at hand that predicts the deformation of the crystal, we determined the magnitude and sign of the surface stress originated by the copper film and its dependence on the thickness.

The surface stresses shown in Table 1 were estimated by using the mean strains observed at the mirror top,  $\bar{\epsilon}_{xx}^{\text{top}}(t_{\text{Cu}}) = \Delta L/L$ , where  $L = 30$  mm is the length of the moiré images, in the nomogram shown in Fig. 12 (black line), which gives the same mean strains evaluated using the digital-twin data as a function of the surface stress. The mean strains  $\epsilon_{xx}^{\text{top}}$

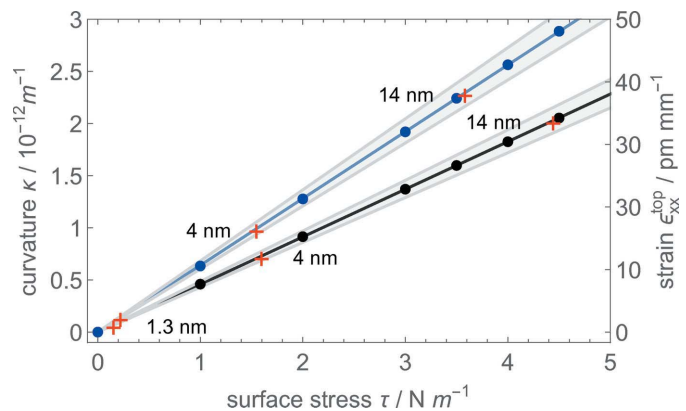


**Figure 12**  
Mean strains  $\bar{\epsilon}_{xx}^{\text{top}}$  at the crystal top (black dots) and curvatures  $\kappa$  (blue dots) of the polynomial regressions and hyperbolic paraboloids best fitting the simulated lattice displacements. The red crosses are the intersections of mean strains and curvatures [obtained from the  $t_{\text{Cu}} = (1.3, 4, 14)$  nm experimental data] with the linear regressions best fitting the digital-twin data (solid lines). The filled areas represent the mean strains and curvatures when the mirror thickness varies from 0.75 to 0.85 mm.

given in Table 1 were obtained via the optimal regression of the strain data; the associated standard uncertainties were estimated as  $(2)^{1/2}\sigma_u/L$ , where  $\sigma_u$  is the standard deviation of the residuals.

The simulated displacements are well approximated by (rectangular) hyperbolic paraboloids, having the axes rotated by  $45^\circ$  clockwise with respect to the  $x$  and  $z$  axes. They are quadratic surfaces given by the equation

$$u_x(x, z; \tau) = u_0 - \kappa(\tau)(x - x_0)(z - z_0)/2, \quad (6)$$

where  $(x_0 = 14.1, z_0 = -13)$  mm are the coordinates of the centre,  $\tau$  is the surface stress, and  $u_0$  and  $-\kappa^2(\tau)$  are the displacement and Gaussian curvature in the centre, respectively.

The axes of the paraboloids approximating the experimental data might be slightly rotated with respect to those approximating the simulated ones, and their centres displaced somewhat. While the  $x$  and  $z$  axes of the finite element model are parallel to the crystallographic directions (110) and (001), the experimentally determined axes might be rotated and might deviate from being orthogonal, and their origin might be displaced. Furthermore, the assumption of uniform surface stress might not be valid.

To accommodate these degrees of freedom, we observed that the Gaussian curvature  $-\kappa^2(\tau)$  is the only parameter of (6) depending on the surface stress. Also, as shown in Fig. 12,  $\kappa(\tau)$  depends linearly on  $\tau$ .

Furthermore, it is invariant under distance-preserving transformations, thus allowing one to compare misaligned paraboloids. This fact enables  $\tau(t_{\text{Cu}})$  to be estimated via the Gaussian curvatures of the paraboloids best fitting the experimental data.

Therefore, to take the possible misalignments between the setup and finite element model into account, we modelled the experimental images as

$$u_x(x, z) = a_{00} + a_{10}x + a_{01}z + a_{11}xz + a_{20}x^2 + a_{02}z^2, \quad (7)$$

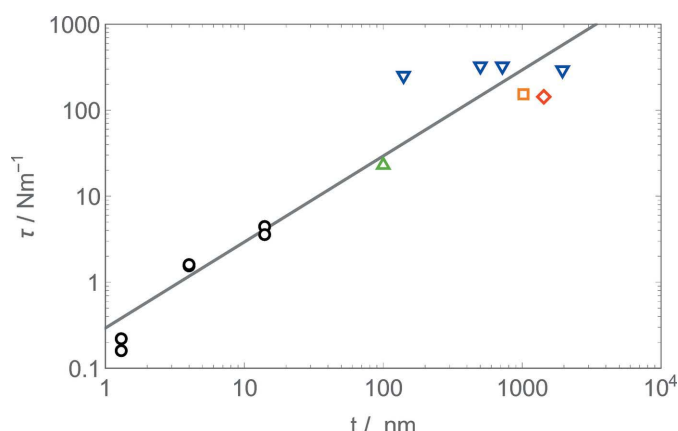


Figure 13

Comparison of our surface-stress values (black dots) with the stress thickness of Cu films on acrylonitrile butadiene styrene (blue triangles), Ni-Fe alloy (orange square), Cu-Fe alloy (red diamond) and SiO<sub>2</sub> (green triangle). Literature data are from the work of Sharma *et al.* (2015, Fig. 4) and Abadias *et al.* (2018, Fig. 1). The black line is the linear regression best fitting our data.

and calculated the curvatures as  $\kappa = (-|H|)^{1/2}$ , where  $H$  is the Hessian of (7) and the vertical bars indicate the determinant. The results are given in the second part of Table 1. The standard uncertainty obtained from the residuals of model (7) was propagated through the  $\kappa$  calculations, also considering that, because of the pixel overlap, the independent data are only 1/8 of the total. Finally, we used the estimated curvatures in the  $\kappa(\tau)$  nomogram, as shown in Fig. 12 (blue line), and found the abscissae  $\tau(t_{\text{Cu}})$  given in Table 1 (second part).

This procedure favours the  $\tau(t_{\text{Cu}})$  values that ensure the best overlap (under a distance-preserving transformation) between the contour lines of the observed and simulated displacement fields. Hence, while the values in the first section of Table 1 have been estimated from the strain at the crystal top only, the values in the second section take the whole strain pattern into account.

The standard uncertainties associated with our  $\tau$  estimates given in Table 1 take only the statistical dispersion of the phase data into account. A more realistic 10% fractional uncertainty follows from the comparison of the estimates based on the mean strain and strain-field curvature.

A survey of the literature suggests that almost three orders of magnitude can be extrapolated from the observed dependence of the surface stress on the film thickness. Fig. 13 compares (in logarithmic scale) our surface-stress values with the stress thicknesses of Cu films on acrylonitrile butadiene styrene, various metals and SiO<sub>2</sub> (Sharma *et al.*, 2015; Abadias *et al.*, 2018).

We do not expect order-of-magnitude differences in the film stresses. In fact, compressive stresses lead to detachment of the layer as a result of buckling. Therefore, adhesion suggests tensile stresses, but if they are too high the film cracks. According to the linear regression of our data, the mean in-plane tensile stress of the Cu film, 0.29 (2) GPa, is independent of the film thickness.

## 6. Conclusions

The accurate measurement of the silicon lattice parameter by X-ray interferometry was a crucial step in counting the atoms in Si spheres – via their unit-cell volumes – for the determination of the Avogadro and Planck constants. It is now essential to the kilogram realization, by reversing the count.

For a 1 kg Si sphere, the effect of the surface stress on the lattice parameter is irrelevant. However, it might not be so for X-ray interferometer crystals, which, typically, are only 1 mm thick. This fact might harm the accuracy of the lattice parameter and unit-cell volume.

We have shown, via phase-contrast imaging of the crystal lattice strains, that the surface finishing has measurable effects on the strain field of the diffracting planes, at the level of a few parts in  $10^9$ .

We coated an interferometer crystal with nanometric Cu films, detected the strains of the diffracting planes and determined the surface stresses explaining them. The resulting mean in-plane stress in the Cu films, 0.29 (2) GPa, is consistent with the stress thickness values given in the literature for

similar interfaces (Sharma *et al.*, 2015; Abadias *et al.*, 2018). We also observe that the strains caused by nanometric Cu films support our fractional 1.25 (72) nm m<sup>-1</sup> correction of the measured lattice parameter (Bartl *et al.*, 2017; Fujii *et al.*, 2017).

Phase-contrast imaging by X-ray interferometry can be used to determine the stress in different films on silicon. Nanometric SiO<sub>2</sub> films better represent the interface of the interferometer crystals, a reconstructed Si layer and an oxide film. Therefore, future work will aim to grow SiO<sub>2</sub> films having known thickness and to measure the associated diffracting-plane strain.

## References

- Abadias, G., Chason, E., Keckes, J., Sebastiani, M., Thompson, G. B., Barthel, E., Doll, G. L., Murray, C. E., Stoessel, C. H. & Martinu, L. (2018). *J. Vac. Sci. Technol. A*, **36**, 020801.
- Apolloni, A., Mana, G., Palmisano, C. & Zosi, G. (2008). *Acta Cryst. A*, **64**, 549–559.
- Bartl, G., Becker, P., Beckhoff, B., Bettin, H., Beyer, E., Borys, M., Busch, I., Cibik, L., D'Agostino, G., Darlatt, E., Luzio, M. D., Fujii, K., Fujimoto, H., Fujita, K., Kolbe, M., Krumrey, M., Kuramoto, N., Massa, E., Mecke, M., Mizushima, S., Mueller, M., Narukawa, T., Nicolaus, A., Pramann, A., Rauch, D., Rienitz, O., Sasso, C. P., Stopic, A., Stosch, R., Waseda, A., Wundrack, S., Zhang, L. & Zhang, X. W. (2017). *Metrologia*, **54**, 693–715.
- Bergamin, A., Cavagnero, G., Mana, G., Massa, E. & Zosi, G. (2000). *J. Phys. D Appl. Phys.* **33**, 2678–2682.
- Bonse, U., Graeff, W. & Materlik, G. (1976). *Rev. Phys. Appl. (Paris)*, **11**, 83–87.
- Camattari, R., Romagnoni, M., Bandiera, L., Bagli, E., Mazzolari, A., Sytov, A., Haaga, S., Kabukcuoglu, M., Bode, S., Hänschke, D., Danilewsky, A., Baumbach, T., Bellucci, V., Guidi, V. & Cavoto, G. (2020). *J. Appl. Cryst.* **53**, 486–493.
- CSC-IT (2020). *Elmer*, <https://www.csc.fi/web/elmer>.
- Ferrari, C., Beretta, S., Rotunno, E., Korytár, D. & Zaprazny, Z. (2020). *J. Appl. Cryst.* **53**, 629–634.
- Fodchuk, I. M. & Raransky, N. D. (2003). *J. Phys. D Appl. Phys.* **36**, A55.
- Fujii, K., Massa, E., Bettin, H., Kuramoto, N. & Mana, G. (2017). *Metrologia*, **55**, L1–L4.
- Heacock, B., Arif, M., Cory, D. G., Gnaeupel-Herold, T., Haun, R., Huber, M. G., Jamer, M. E., Nsofini, J., Pushin, D. A., Sarenac, D., Taminiau, I. & Young, A. R. (2018). *Rev. Sci. Instrum.* **89**, 023502.
- Heacock, B., Haun, R., Hirota, K., Hosobata, T., Huber, M. G., Jamer, M. E., Kitaguchi, M., Pushin, D. A., Shimizu, H., Taminiau, I., Yamagata, Y., Yamamoto, T. & Young, A. R. (2019). *Acta Cryst. A*, **75**, 833–841.
- Kessler, E. G., Owens, S. M., Henins, A. & Deslattes, R. D. (1999). *IEEE Trans. Instrum. Meas.* **48**, 221–224.
- Mana, G., Albo, P. G. & Lago, S. (2014). *Measurement*, **55**, 564–570.
- Mana, G., Massa, E. & Sasso, C. P. (2019). *Metrologia*, **56**, 025003.
- Mana, G. & Palmisano, C. (2004). *Acta Cryst. A*, **60**, 283–293.
- Mana, G. & Vittone, E. (1997a). *Z. Phys. B*, **102**, 189–196.
- Mana, G. & Vittone, E. (1997b). *Z. Phys. B*, **102**, 197–206.
- Massa, E., Sasso, C. P., Mana, G. & Palmisano, C. (2015). *J. Phys. Chem. Ref. Data*, **44**, 031208.
- Melis, C., Giordano, S., Colombo, L. & Mana, G. (2016). *Metrologia*, **53**, 1339–1345.
- Mendel, E. & Yang, K. H. (1969). *Proc. IEEE*, **57**, 1476–1480.
- Miao, H., Panna, A., Gomella, A., Bennett, E., Znati, S., Chen, L. & Wen, H. (2016). *Nat. Phys.* **12**, 830–834.
- Ohler, M., Köhler, S. & Härtwig, J. (1999). *Acta Cryst. A*, **55**, 423–432.
- Pushin, D. A., Cory, D. G., Arif, M., Jacobson, D. L. & Huber, M. G. (2007). *Appl. Phys. Lett.* **90**, 224104.
- Quagliotti, D., Mana, G., Massa, E., Sasso, C. & Kuetgens, U. (2013). *Metrologia*, **50**, 243–248.
- Sharma, T., Brüning, R., Nguyen, T. C. L., Bernhard, T. & Brüning, F. (2015). *Microelectron. Eng.* **140**, 38–46.
- Zawisky, M., Springer, J., Farthofer, R. & Kuetgens, U. (2010). *Nucl. Instrum. Methods Phys. Res. A*, **612**, 338–344.